Journal of Electroanalytical Chemistry 892 (2021) 115309

Contents lists available at ScienceDirect

Journal of Electroanalytical Chemistry

journal homepage: www.elsevier.com/locate/jelechem

Tracking the evolution of processes occurring in silicon anodes in lithium ion batteries by 3D visualization of relaxation times

Erick Espinosa-Villatoro [a], Johanna Nelson Weker [b], Jesse S. Ko [b,*], Enrique Quiroga-González [a,*]

[a] Institute of Physics, Benemérita Universidad Autónoma de Puebla (BUAP), 72570 Puebla, Mexico
[b] Stanford Synchrotron Radiation Lightsource, SLAC National Accelerator Laboratory, Menlo Park, CA, USA

ARTICLE INFO

Keywords:
Lithium-ion battery
DRT
Impedance spectroscopy
Silicon anode
Solid electrolyte interphase

ABSTRACT

An unconventional electroanalytical method has been used for tracking processes in silicon anodes in lithium ion batteries: a 3D visualization of relaxation times. Impedance data of the electrodes were collected at different potentials and different cycles during cyclic voltammetry, and were treated by means of the Distribution of Relaxation Times (DRT) method. A 3D visualization of the results allowed to identify the formation of a solid electrolyte interphase on the anode, composed of two layers with different relaxation times. Such findings are not possible by conventional analysis of impedance data by modeling with equivalent circuits, nor by simple DRT alone. Additionally, it was possible to observe that the characteristic relaxation time of the lithiation of the Si anode becomes smaller upon cycling, indicating that the material experiences structural transformations that allow it to lithiate faster. This result is relevant to motivate the use of micron-sized particles in the anode.

1. Introduction

Rechargeable batteries exhibit a myriad of physicochemical processes related to distinct events occurring at the electrode–electrolyte interface [1]. Interfacial processes govern the longevity and electrochemical performance of rechargeable batteries; thus, it is necessary to accurately assess reactions that take place at this electrode–electrolyte interface [1]. Among the various types of rechargeable battery systems, lithium-ion batteries (LIBs) continue to be the subject of intense research because of their widespread applications [2–5]. The understanding of the complex interplay between the anode, cathode, and electrolyte is essential to advance LIB technology. In particular, the formation of a stable solid electrolyte interphase (SEI) layer at the anode plays a crucial role in the reversible electrochemical behavior [6].

Ongoing research is dedicated to producing active materials with higher capacities coupled with stable cycling. Silicon is an attractive anode due to its high gravimetric capacity (4200 mAh g^{-1} for $Li_{22}Si_5$ at high temperature (~325 °C) and 3580 mAh g^{-1} for $Li_{15}Si_4$ at room temperature), which is ten-fold higher than graphite (372 mAh g^{-1}) [7–12]. Moreover, Si is appealing because it is the second most abundant element in the Earth's crust, it is environmentally friendly, and it has a low electrochemical potential (~0.37 V *vs.* Li/Li^+) [13–16]. However, the main drawback to adopting Si as an anode is that the volume change (> 300%) during cycling generates significant mechanical stress that commonly cracks and pulverizes the particles in just a few cycles, which ultimately leads to significant capacity fade [17]. This large volume change in silicon results in another issue-the formation of an unstable SEI layer. It is desirable that the SEI layer is dense, stable, and provides high ionic conductivity [8,18]. To address these problems, nano- and micro-structured Si has been recently developed, as well as nanostructured Si composites, such as Si-carbon, Si-metal, Si-transition metal oxides, and Si-polymer. Although recent efforts have focused on Si nanoengineering, it is also important to consider the use of micron-sized particles, for advantages in processibility. In this sense, it has been demonstrated that Si microwires with an optimized geometry present an exceptional performance as anode material in lithium-ion batteries, with the advantage of a lower production cost compared to nanostructured Si [6,19–22,52].

The performance of LIBs is in large part affected by interfacial processes, and it is now well understood that the decomposition of the organic electrolyte leads to a stable SEI on graphite, but not on Si. Yet, attempts to understand the evolution of the SEI upon cycling still remains to be fully comprehended [23–27] To understand the complex dynamics of the SEI on Si, vast efforts that include X-ray characterization, neutron-based methods, and infrared-based techniques have recently been used [28]. For instance, Cao *et al.* combined in situ X-ray reflectivity, ex situ X-ray photoelectron spectroscopy, linear

* Corresponding authors.
E-mail addresses: jesse.ko@jhuapl.edu (J.S. Ko), equiroga@ieee.org (E. Quiroga-González).

https://doi.org/10.1016/j.jelechem.2021.115309
Received 3 February 2021; Received in revised form 10 March 2021; Accepted 23 April 2021
Available online 28 April 2021

sweep voltammetry and first principles calculations to study the formation of the SEI layer for a Si anode [29]. Their results showed the formation of two well-defined layers of SEI layer: an "inorganic SEI" layer comprising a bottom-SEI layer at the Si/SEI junction, which results from the lithiation of the native oxide, and an "organic-SEI" layer on top the "inorganic SEI" layer at the bottom-SEI/electrolyte interface.

Electroanalytical techniques are complementary for understanding interfacial processes in an electrochemical cell like a lithium-ion battery. Electrochemical impedance spectroscopy (EIS) is a nondestructive tool for the analysis of the polarization behavior of electrochemical systems in the frequency domain [30]. By studying the behavior of electrochemical processes with EIS, one can study complex systems characterized by multiple timescales by extracting various time constants associated for a given process [20]. Typically, impedance data are fitted using an equivalent circuit model (EC-model), which provides values of the elements and, hence, the physical characteristics. Yet, the choice of an appropriate EC requires prior knowledge of the impedance of each element, which may be difficult to assign. For example, Hansen *et al.* showed that by using an appropriate EC model, it is possible to extract time constant values ($\tau \equiv RC$) and directly correlate those values to the phase transformations in Si microwires (μW-Si) with in situ Fast-Fourier-Transform Impedance Spectroscopy and voltammetric data [31]. According to their results, the fastest process (lowest τ) arises from the electrolyte interaction with the carbon-composite matrix of the μW-Si electrodes. The next fastest process then corresponds to the formation of the SEI layer, which is formed in the first cycle. The slowest process then correlates to the charge transfer in the μW-Si electrode. With the aforementioned assumptions of the physical characteristics of the μW-Si electrode, it was possible to extract characteristic τ time values for these distinct interfacial processes.

To complement EIS analysis, the distribution of relaxation time (DRT) method provides an alternative approach to analyzing EIS data [32–35]. The DRT method is a complementary electroanalytical tool used to interpret an electrochemical system as a continuous distribution of RQ elements as a function of relaxation times (Fig. 3) [22–24,35]. This method offers direct access to a distribution of time constants of the system under study in the time scale, rather than discrete values. The DRT analysis has found recent success for understanding electrochemical processes associated with fuel cells [36–40] and batteries [41–43]. In particular, the Ciucci group has recently advanced this analysis by proper regularization and fitting of impedance data, while verifying their techniques by correlating both theory and experiment [44–47]. Thus far, the DRT method has mainly been used at particular charged/discharged states of a battery as a single-point measurement [31–33]. In the present study, it was chosen to study bulk micro-Si-carbon composite electrodes in a LIB configuration, while acquiring impedance spectra at small increments of voltage throughout the entire voltage range (0.02–1.0 V *vs.* Li/Li^+) during cyclic voltammetry. The addition of a third independent variable, the voltage, allows one to observe gradual changes in the time response of the electrochemical system in three dimensions. This method of representing DRT-derived data in three dimensions allows to map out both time-dependent (frequency or time constant) and potential-dependent processes in high resolution. The Si electrodes serve as a model system with which to study the dynamic processes which evolve as a function of cycle number, where pulverization, crystalline-to-amorphous transitions, and SEI growth all contribute greatly to the impedance response. The purpose of the present study is to use impedance spectroscopy as a means to investigate these complicated processes occurring in silicon anodes while being charge/discharge cycled. The described technique could become complementary to other techniques, such as in situ X-ray reflectivity, scanning Electron Microscopy, X-ray diffraction, and cyclic voltammetry [14,22,48,53].

2. Experimental

Slurries were prepared by mixing commercial Si powder (Alfa Aesar, APS 1–5 μm, 99.9%) with conductive carbon (Super P) and sodium carboxymethyl cellulose (Sigma-Aldrich, average $M_w \sim 90{,}000$) in a ratio of 3:6:1 with de-ionized water (18 MΩ cm). This slurry was then coated onto a 9-μm thick copper foil (MTI corporation, >99.99%) and subsequently dried at 80 °C for 24 h under vacuum. The large amount of conductive carbon was used to minimize limitations in the electronic transport to the Si particles, to be able to relate the observations to ionic transport and electrochemical processes.

All electrochemical tests were performed using a metallic lithium as a counter electrode in stainless steel CR2032 coin cells, in which a Whatman glass fiber separator (GF/C) was soaked in 200 μL of LP30 electrolyte (1 M $LiPF_6$ in EC:DMC 50:50 v:v, Sigma-Aldrich). Cyclic voltammetry was performed at a scan rate of 0.1 mV s^{-1} in a voltage range from 0.02 to 1.0 V *vs.* Li/Li^+. Stepped electrochemical impedance spectroscopy (SPEIS) was performed within a frequency range of 10 mHz − 200 kHz using a small AC signal of 10 mV. Impedance data were collected across the entire voltage range in 20 mV increments (51 total EIS scans). The data were fitted with an EC-model of a series resistor and three RQ (where R is the resistance and Q is a constant phase element) circuits, using the EC-Lab® software from Bio-Logic, in agreement with reported work on Si anodes [12,49]. For many analyses of the present work, three representative voltages were chosen from the highest, medium, and lowest voltage regions: 0.98 V, 0.48 and 0.04 V, respectively.

The DRT analysis was used to identify characteristic distribution of typical EIS timescales where the experimental data were fitted against a model (Z_{DRT}), which is obtained from the following relationship [35]:

$$Z_{DRT}(f) = R_\infty + \int_0^\infty \frac{g(\tau)}{1 + i2\pi f\tau} d\tau \quad (1)$$

where R_∞ is the ohmic resistance, and $g(\tau)$ represents the reactive impedance as a function of relaxation times τ (impedance distribution in the time scale), and f is the frequency. The τ and f are related by the expression:

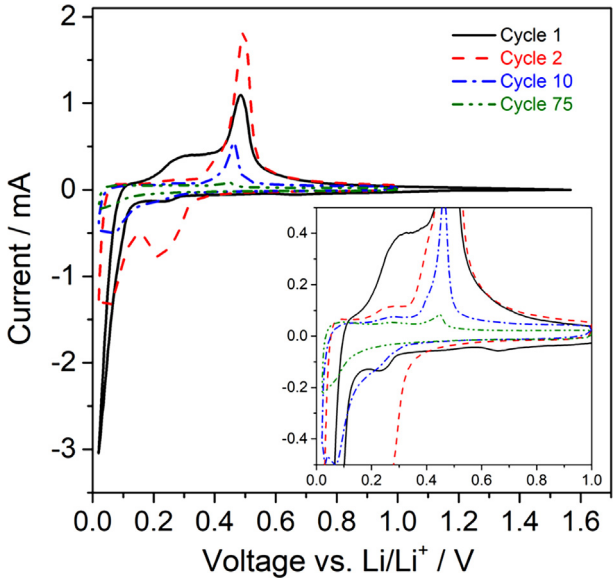

Fig. 1. Cyclic voltammogram of Li//Si cells cycled for 75 cycles from 0.02 to 1.0 V *vs.* Li/Li^+ in 1 M $LiPF_6$ in EC:DMC.

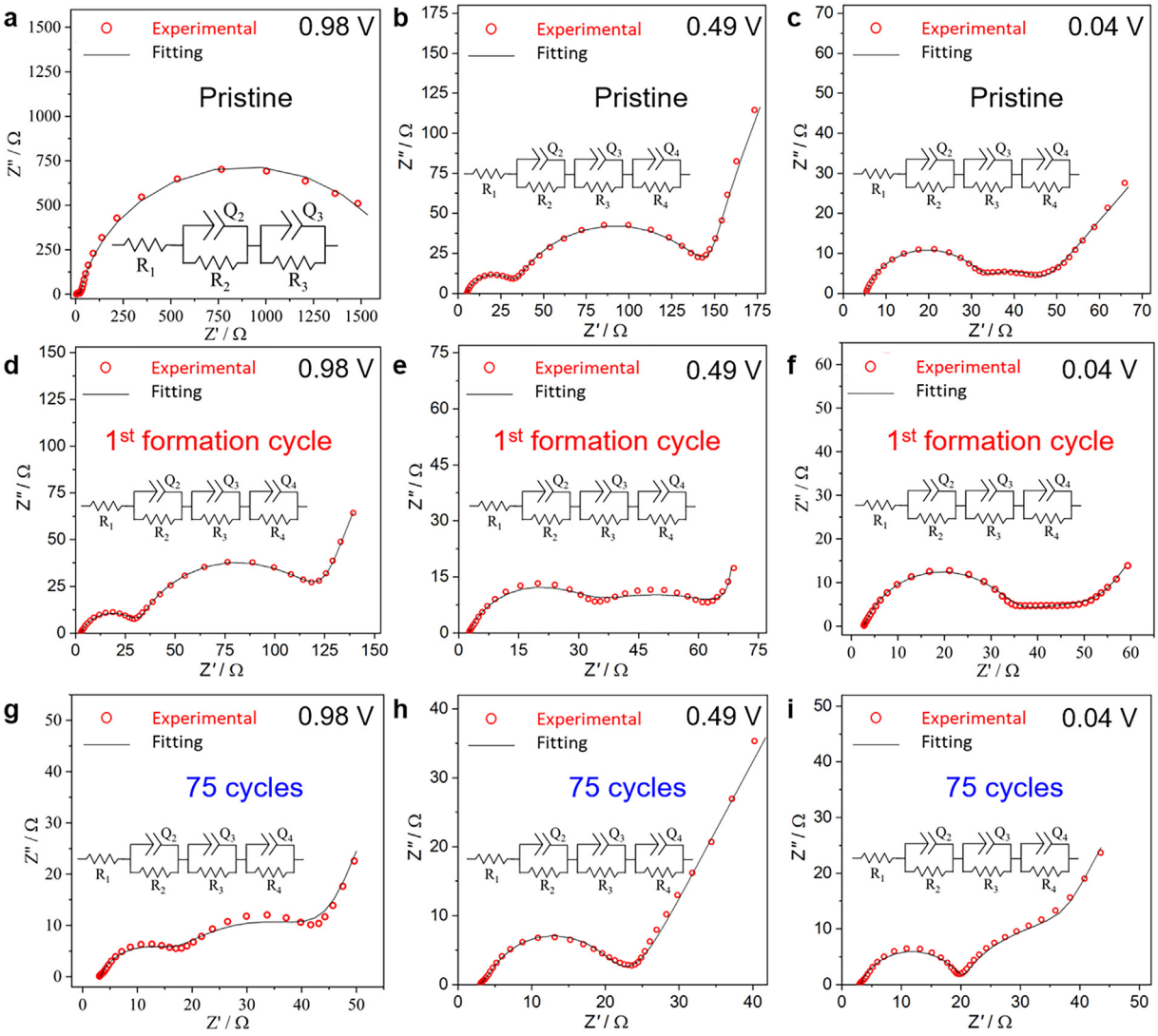

Fig. 2. Nyquist plots of Li//Si cells in their (a–c) pristine state, (d–f) after one formation cycle, and (g–i) after 75 cycles. Impedance data were collected at 0.98, 0.49, and 0.04 V. The red circles correspond to the experimental data while the black lines correspond to the equivalent circuit fitting. The equivalent circuit used in each fitting can be seen in the embedded figure of each measurement.

$$\tau = \frac{1}{2\pi f} \tag{2}$$

The Matlab GUI, DRTtools, developed by Ciucci *et al.* was used for fitting our impedance data based on the Tikhonov regularization [35]. In this way, Eq (1) can then be expressed as [35]:

$$Z_{DRT} = R_{\infty} + \int_{-\infty}^{\infty} \frac{\gamma(ln\tau)}{1 + i2\pi f\tau} dln(\tau) \tag{3}$$

where $\gamma[\ln(\tau)] = \tau g(\tau)$; $\ln(\gamma(\tau))$ is then another representation of the distribution of relaxation times.

3. Results and discussion

The morphology of the carbon-composite electrode comprising silicon powder, conductive carbon, and polymeric binder was investigated with scanning electron microscopy (Fig. S1a,b, in supplementary information). The heterogeneous electrode architecture exhibits a Si particle size distribution of 1–5 μm (Fig. S1a). At higher magnification, we observe the morphology of the Si particles that are well-dispersed within the carbon-composite matrix (Fig. S1b). Morphological changes occurring cycling have been already thoroughly studied, as in the work of H. Cheng et al. [50], D. Yao et al. [51], K. Zhang et al. [52], serving as a reference to correlate with the electrochemical results of the present work. The Si electrodes paired with Li metal (Li//Si) were first assessed by cyclic voltammetry (CV) to observe key oxidation/reduction features (Fig. 1). The voltammetric features are similar to previously reported studies on Si [53,54]. During the first cycle, the peak at ~ 0.63 V is attributed to the formation of a solid electrolyte interphase layer, and the peak at ~ 0.22 V corresponds to the formation of a Li-Si alloy ($Li_{13}Si_4$ phase; inset in Fig. 1) [12,40]. In the second cycle, two peaks are observed during the lithiation process that correspond to the formation of *c*-$Li_{22}Si_5$ (~0.05 V) and the transformation to new phase of *a*-$Li_{22-x}Si_5$ (~0.025 V) due to the formation of crystalline core and an amorphous shell in the Si particles according to S.-Y. Lai's work [40,42,55]. Upon delithiation, two peaks appear at ~ 0.3 V and ~ 0.5 V, which correspond to the partial extraction of Li from Li_xSi_y phases and the complete extraction of Li from Si, respectively [39,40,56,57]. During the first few cycles one can observe that the intensity of the peaks at ~ 0.22 and 0.05 V (lithiation) and 0.5 V (delithiation) increase, what is normal, considering that during the first cycle Si is becoming amorphous, and every cycle it is possible to lithiate a bit more [15]. For large Si particles of hundreds to thousands of nm, it is common that

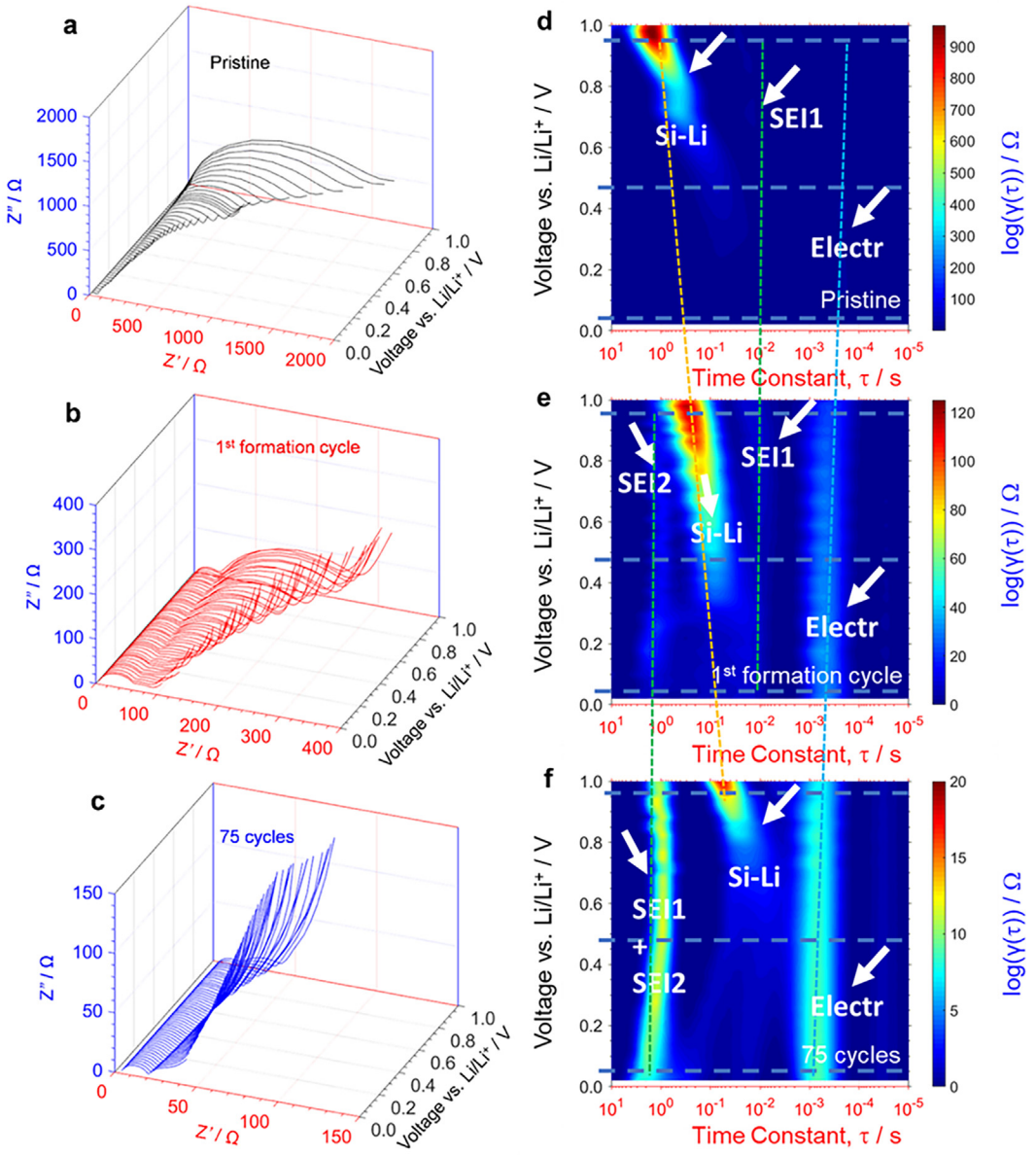

Fig. 3. The (a–c) 3D Nyquist plots collected from 0.02 to 1.0 V *vs.* Li/Li^+ for Li//Si cells measured in its (a) pristine state, (b) after 1st formation cycle, and (c) after 75 cycles. Color-mapped DRT plots of $\gamma(\tau)$ *vs.* time constant and voltage for Li//Si cells measured in its (d) pristine state, (e) after 1st formation cycle, and (f) after 75 cycles.

Table 1
Tabulated values of the time constants (τ) calculated from the Nyquist plots from equivalent circuit fitting.

Cycle History	Component	Time constant, τ (s)		
		0.98 V	0.49 V	0.04 V
Pristine	Electrode	82.4	119	223
	SEI	–	0.130	7.18×10^{-2}
	Electrolyte	3.67×10^{-4}	7.95×10^{-4}	8.72×10^{-4}
1st Formation Cycle	Electrode	123	226	131.4
	SEI	0.206	0.189	0.679
	Electrolyte	27.5×10^{-4}	16.5×10^{-4}	10.9×10^{-4}
75 Cycles	Electrode	233	206	87.7
	SEI	0.120	0.107	1.62
	Electrolyte	29.4×10^{-4}	15.7×10^{-4}	38.6×10^{-4}

the material is not completely lithiated in a voltammetric cycle [13]. On the other hand, as the time per cycle is short in voltammetry, limiting the lithiation depth, the particles are just stressed in shallow depths, causing cracks and deactivation of Si pieces and consequently intensity fade upon prolonged cycling. Furthermore, the apparent low efficiency between the first and second voltammetric cycle is quite

Table 2
Tabulated values of the time constants (τ) calculated from the DRT analysis (Fig. 3).

Cycle History	Component	Time constant, τ (s)		
		0.98 V	0.49 V	0.04 V
Pristine	Electrode	1.6	0.1	2
	SEI	3.0×10^{-2}	2.85×10^{-2}	9.9×10^{-2}
	Electrolyte	0.4×10^{-4}	1.9×10^{-4}	2.2×10^{-4}
1st Formation Cycle	Electrode	0.29	0.12	0.19
	SEI 1	1.5×10^{-2}	0.89×10^{-2}	2.1×10^{-2}
	SEI 2	0.11	0.9	1.9
	Electrolyte	4.1×10^{-4}	4.9×10^{-4}	4.6×10^{-4}
75 Cycles	Electrode	5.2×10^{-2}	3.8×10^{-2}	1.8×10^{-2}
	SEI	1.13	0.98	2.1
	Electrolyte	6.5×10^{-4}	7.1×10^{-4}	6.9×10^{-4}

common for micron-sized Si anodes, related to SEI layer formation. What occurs is that the Si lithiation does not only occur at specific voltages, but is distributed over the entire voltage range, as can be evidenced by the change in the time constant of Si lithiation with varying voltage (see Fig. 3d–f). This variation is largest in the first cycle [14,15,18,23,24,58]. The area under the curve in the negative voltage sweep is close to the area under the curve in the positive voltage sweep.

To understand the dynamic processes that occur; such as electrode degradation, formation of an SEI layer, and electrolyte decomposition; and how they affect the total impedance response of the Li//Si cells during cycle, Nyquist plots of three cells with different cycling histories were analyzed: pristine, after one cycle (formation cycle), and after 75 cycles. (Fig. 2). It was used an equivalent circuit of a series resistance and two RQ for the first pristine state, and a series resistance and three RQ circuits for the rest of the cases, in accordance with related work on Si anodes [12,21,48,59] to fit the impedance spectra through an iterative algorithm of the software EC-Lab of BioLogic. The values obtained from fitting were attributed to the SEI layer, charge-transfer, and electronic contact between the current collector and anode components, which include the Si particles, binder, and conductive carbon [21,44]. Nyquist plots at three different DC voltages of 0.98, 0.49, and 0.04 V were chosen for this study. At 0.98 V, the electrode is in its fully charged state (delithiated). At 0.49 V, a SEI layer has formed during the first cycles, and it is the potential before the alloying of Li with Si. Finally, at 0.04 V, Si has alloyed with Li^+.

For all three samples (pristine, 1st formation cycle, and 75 cycles), the changes in the diameter of the semicircles of the Nyquist plots are evident at all DC voltages selected (Fig. 2), which qualitatively indicates changes in the ohmic resistances associated to the different processes. The time constants calculated from the R and Q values (time constant τ = RQ) derived from the EC-fits are reported in Table 1. With τ one can distinguish distinct processes from their associated electrochemical time scale. The slowest time constant can be associated with charge transfer in the Si anode (τ_{Si}). The formation of the SEI layer around the Si particles can be related to another RQ element, expressed as τ_{SEI}. The fastest process is related to the charge transport in the electrolyte ($\tau_{electrolyte}$) [12,21,32]. Table 1 summarizes all the values of the τ assigned to the contributions at the different components such as Si, SEI layer, and electrolyte at each voltage. The R and Q values can be found in Tables S1–S3.

As can be seen for the pristine anode at 0.98 V (see Table 1), the cell exhibits high impedance at low frequencies of Z_{tot} = ~1800 Ω, probably due to the presence of a native SiO_2 layer (Fig. 2a) [19,60]. At 0.49 V, according to Cao's work, the SEI layer has now formed. At 0.7 V, the inorganic-SEI is formed into lithium silicides (Li_xSi) and lithium silicates (Li_xSiO_y). In addition, at 0.6 V, the organic-SEI is formed, which consists mainly of the electrolyte decomposition products [21–23,61], resulting in a smaller Z_{tot} of 1180 Ω (Fig. 2b). At 0.04 V, a further increase in Z_{tot} to 1480 Ω (Fig. 2c) is observed, as a result of the formation of a Li-Si alloy which is confirmed by CV analysis.

In a separate study, after the Li//Si cell undergoes the 1st formation cycle, changes in the semicircles are also evident (Fig. 2d–f). Of note, we assume that an unstable SEI layer [8] has already formed during the cycle prior to the EIS measurements. Interestingly, Z_{tot} at 0.98, 0.49, and 0.04 V are smaller compared to those observed for the pristine cell (Table S2). We attribute this reduction in Z_{tot} to the amorphization of the Si particles [14,18,41,62]. Finally, the fitted Nyquist plots of Li//Si cell cycled up to 75 cycles are presented in Fig. 2g–i. At 0.98 V one can observe an increase in the Z_{tot}, but a slight decrease in the capacitance of the Si-Li element (Table S3), however, it is observed that at 0.49 V the Z_{tot} decreases, once a new SEI layer has formed, to finally find the lowest Z_{tot} of 121.3 Ω at 0.04 V corresponding to the Si/Li alloy [21,46,47].

In the calculation of τ obtained at 0.98 V for the pristine Li//Si cell, two RQ and a series resistance were used. The slowest τ is associated with the Si electrode (τ_{Si} and $\tau_{Si\text{-}Li}$) and the faster process is related to the charge transfer through the electrolyte ($\tau_{electrolyte}$) [12,63]. On the other hand, at 0.49 V an additional RQ element was added to the equivalent circuit, which is related to the initial formation of a SEI layer [19]. The τ_{SEI} at 0.04 V decreases to 7.18×10^{-2} s. The $\tau_{electrolyte}$, which is related to the ionic conduction associated with the charge transport through the electrolyte, remains in the same order-of-magnitude in the three voltages analyzed. The τ_{Si} at 0.98 V yields a low value of 82.4 s and at 0.49 V increases to 119 s. At 0.04 V, the particles now comprise of a Li-Si alloy in addition to a SEI layer, and $\tau_{Si\text{-}Li}$ increases to 223 s.

For the Li//Si cell after the 1st formation cycle, τ_{SEI} remains nearly constant at 0.98 V and 0.49 V (0.206 s and 0.189 s, respectively), but at the alloying voltage (0.04 V), τ_{SEI} increases slightly to 0.679 s, suggesting changes in the SEI layer at this low voltage. Similar to the pristine Li//Si cell, $\tau_{electrolyte}$ remains in the same order-of-magnitude at all three voltages. For the charge transfer to the Si particles, $\tau_{Si\text{-}Li}$ is also nearly constant with values ranging from 123 to 226 s and at 0.04 V, shows a time constant of 131.4 s. This is likely due to the formation of Li-Si alloys [12,40].

The time constants were evaluated also after 75 cycles, to gain certain insight into the structural changes occurring upon cycling, and possible capacity fading [7,9,46,64]. It is clear that cyclic voltammetry is not the proper technique for studying aging, but after tens of cycles some aging is reached. The calculation of the τ_{SEI} at 0.98 V in this Li//Si cell has a value of 0.120 s. At 0.04 V, a high τ_{SEI} of 1.62 s is yielded, indicating the possibility that continuous SEI growth has occurred during prolonged cycling. Moreover, it was identified that $\tau_{electrolyte}$ still remains in the same order-of-magnitude at the three voltages even after 75 cycles. The $\tau_{Si\text{-}Li}$ at 0.98 V exhibits a slow time constant of 233 s, while at 0.49 V it decreases to 206 s, and at 0.04 V it is 87.7 s.

The associated τ values derived from the DRT analysis are summarized in Table 2, and can be visualized in Fig. S2. The values derived from both techniques are comparable. However, one needs to consider that there is about 1 order of magnitude of difference between them, due to the nature of the techniques. The DRT shows the onset

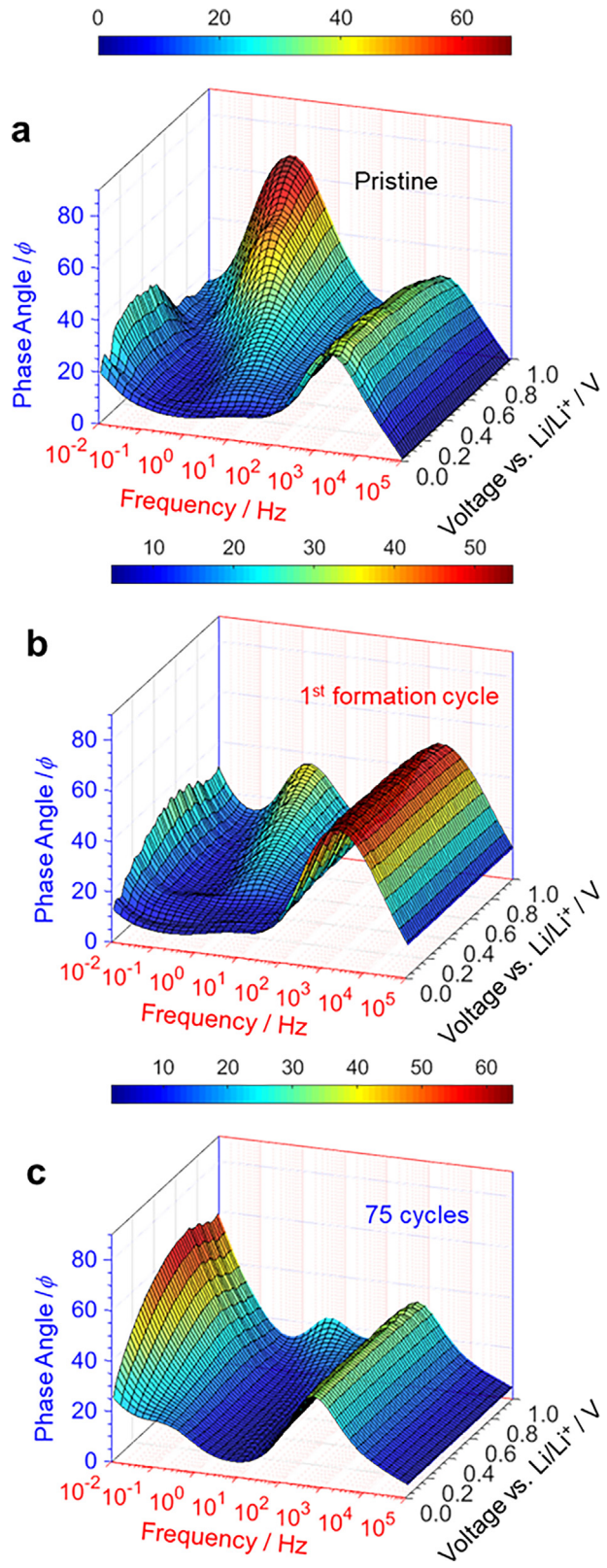

Fig. 4. The 3D Bode plots of the phase angle (ϕ) *vs.* the frequency and voltage of Li//Si cells in its (a) pristine state, (b) after 1st formation cycle, and (c) after 75 cycles. The color bar for eot represents the magnitude of the ϕ values.

frequency (relaxation time) of changes in impedance, while the values obtained by EC-fitting are about the frequency at maxima of impedance; additionally, there is certain level of deviation due to the regularization parameters used for the DRT analysis [35]. The additional information that could be gained by DRT is the discovery of an extra time constant in the order of 10^{-2} s. This time constant appear even in the pristine electrode at 0.98 V, this it can be associated either to the conductive matrix containing Si particles [12,44] or most probably to the native SiO_2 layer [19]. This time constant remains even at 0.49 V, when the SEI layer has formed, but no additional time constants appear. This may indicate that the native SiO_2 becomes part of the SEI; then the SEI may be inorganic in large extent during the first cycle. During the second cycle (1st formation cycle), and additional SEI layer appear (SEI 2), which is one order of magnitude slower. This could be associated to the organic part of the SEI.

The distribution of relaxation times, $\gamma(\tau)$, derived from all the impedance data (Fig. 3a–c) were mapped out in greater detail in 3D as the color-mapped plots of Fig. 3d–f. For these plots, the impedance data were collected across the entire voltage range in 20 mV increments. In them, the most representative changes are marked with white arrows, and dotted lines show the trend of each of the components. After the 1st formation cycle (Fig. 3e), one can observe two contributions related to the τ_{SEI} (SEI 1 and SEI 2 in Table 2), where $\tau_{SEI\ 1} = 1.5 \times 10^{-2}$ s and $\tau_{SEI\ 2} = 0.11$ s (at 0.98 V), $\tau_{SEI\ 1} = 0.89 \times 10^{-2}$ s and $\tau_{SEI\ 2} = 0.9$ s (at 0.49 V), and $\tau_{SEI\ 1} = 2.1 \times 10^{-4}$ s and $\tau_{SEI\ 2} = 1.9$ s (at 0.04 V). These lines in Fig. 3e of τ_{SEI} clearly indicate that there exist several contributions to the SEI layer formation, which include an inorganic and organic layer [19]. A different 3D visualization of the data is shown in Fig. S3, to corroborate the existence of two SEI signals. The $\tau_{electrolyte}$ remains nearly constant at a value of ~ 4×10^{-4} s. Moreover, the Si particles also exhibit consistent τ_{Si} values (~0.2 s) at the three different voltages.

After 75 cycles, one can observe just one time constant related to SEI (τ_{SEI}); then, it is possible to infer that the contributions associated to the SEI 1 and SEI 2 merge (Fig. 3f). The overall τ_{SEI} values for this Li//Si cell are higher compared to the pristine and 1st formation cycle cells, indicating that SEI becomes more isolating upon cycling (has a higher organic contribution). The SEI grows until a stable layer is formed, if the voltage limits for cycling are properly set, as previously reported [15,54]. The mainly organic nature of SEI after long cycling has been evidenced in different work, like the one of Veith *et al.* [64]. In the present work, after 75 voltammetry cycles, once the Li//Si cell has reached a stationary state, τ_{SEI} corresponding to the organic and inorganic phase are mixed, with time constant closer to the one of the organic contribution (τ_{SEI} ~ 1 s).

On the other hand, a slight increase in the $\tau_{electrolyte}$ is also exhibited. The value is ~ 7×10^{-4} s. This increase in $\tau_{electrolyte}$ suggests that there is also degradation of the liquid electrolyte with prolonged cycling. Interestingly, τ_{Si} changes very slightly from the 1st formation cycle to 75 cycles, indicating that the formed Li-Si phases have similar properties upon cycling after the first cycle (after amorphization).

Based on the range of τ values as a function of f, it is also possible to investigate the kinetics of the aforementioned processes by analyzing the changes in the phase angle (ϕ), which is yet another parameter that represents time-dependent processes. In recent studies, the 3D Bode analysis was used to understand charge-storage kinetics by representing the phase angle (ϕ) to the frequency and potential in three-dimensions to assess the kinetic properties of electrochemical energy storage [65,66,67]. A ϕ of 90° corresponds to an ideal capacitive behavior (*e.g.,* parallel-plate capacitor) while a ϕ of 45° indicates a diffusion-controlled process, and $\phi < 45°$ resembles a resistive process [20]. The 3D Bode plots representing the ϕ as the dependent variable (Fig. 4) shows strong correlation to the τ values exhibited in the 3D DRT plots (Fig. 3). For the pristine Li//Si cell, there is a high ϕ contribution (~65°) within a frequency range (f) from 1 to 100 Hz (Fig. 4a). This region of the SEI layer initially shows fast kinetics, but this value decreases to ~ 40° after the 1st formation cycle (Fig. 4b) and further decreases to ~ 20° after 75 cycles (Fig. 4c). Moreover, as the ϕ continues to decrease within the SEI region, the ϕ at the low frequency region (slow τ), corresponding to the Si particles, increases with prolonged cycling (Fig. 4a–c). This indicates that the

Si particles become amorphous, showing a more kinetically favorable lithiation process [41]. Interestingly, the ϕ values for the electrolyte remain constant ~ 45° for all three cases (Fig. 4a–c), indicating that this interfacial process is limited by electrolyte diffusion to the active material.

4. Conclusions

Visualizing relaxation times of Si anodes in batteries in a 3D plot has enabled to track their evolution during cycle voltammetry tests, even with details rarely observable by conventional impedance analysis by EC-modeling. In particular, this technique identified the formation of the solid electrolyte interphase, which is constituted by two layers: an inorganic phase, formed parting from a native SiO_2 layer, and an organic phase, formed by decomposition products of the electrolyte, which yields a slower time constant. Additionally, a clear structural change of the anodes could be inferred, within each voltammetry cycle (different Si-Li phases form) and from cycle to cycle. The time constant related to the charge transfer to the Si anodes becomes faster from cycle to cycle, tending towards a stationary state. The values of relaxation times obtained by DRT are comparable to the ones obtained by EC-fitting, but shifted one order of magnitude, due to the nature of the techniques. 3D visualization of DRT data can be considered an advanced technique, providing further mechanistic insights into the complex charge-storage processes associated with silicon anodes.

Declaration of Competing Interest

The authors declare that they have no known competing financial interests or personal relationships that could have appeared to influence the work reported in this paper.

Acknowledgements

The authors thank the facilities provided by Stanford Synchrotron Radiation Lightsource, SLAC National Accelerator Laboratory, which is supported by the U.S. Department of Energy, Office of Science, Office of Basic Energy Sciences under Contract No. DE-AC02-76SF00515. The author E.E.-V. acknowledges the financial support of CONACyT through under Award #582796.

Contributions

E.E.-V. and J.S.K. performed the experiments, cured data, analyzed data and wrote the first draft. J.N.W. acted as advisor in the project and revised the manuscript. E. Q.-G. acted as advisor in the project, analyzed data and revised the manuscript.

Appendix A. Supplementary data

Supplementary data to this article can be found online at https://doi.org/10.1016/j.jelechem.2021.115309.

References

[1] J.B. Goodenough, Y. Kim, Challenges for rechargeable Li batteries, Chem. Mater. 22 (2010) 587–603.
[2] N. Nitta, F. Wu, J.T. Lee, G. Yushin, Li-ion battery materials: present and future, Mater. Today 18 (2015) 25–264.
[3] M. Winter, B. Barnett, K. Xu, Before Li ion batteries, Chem. Rev. 118 (2018) 11433–11456.
[4] M. Li, J. Lu, Z. Chen, K. Amine, 30 years of lithium-ion batteries, Adv. Mater. 30 (2018) 1800561.
[5] J. Wang, T. Xu, X. Huang, H. Li, T. Ma, Recent progress of silicon composites as anode materials for secondary batteries, RSC Adv. 6 (2016) 87778–87790.
[6] J. Zhang, C. Zhang, S. Wu, J. Zheng, Y. Zuo, C. Xue, C. Li, B. Chen, High-performance lithium-ion battery with nano-porous polycrystalline silicon particles as anode, Electrochim. Acta 208 (2016) 174–179.
[7] Y. Jin, B. Zhu, Z. Lu, N. Liu, J. Zhu, Challenges and recent progress in the development of Si anodes for lithium-ion Battery, Adv. Energy Mater. 7 (2017) 1700715.
[8] Y. He, X. Yu, G. Li, R. Wang, H. Li, Y. Wang, H. Gao, X. Huang, Shape evolution of patterned amorphous and polycrystalline silicon microarray thin film electrodes caused by lithium insertion and extraction, J. Power Sources 216 (2012) 131–138.
[9] W.F. Ren, Y. Zhou, J.T. Li, L. Huang, S.G. Sun, Si anode for next-generation lithium-ion battery, Curr. Opin. Electroche. 18 (2019) 46–54.
[10] D.W. Choi, K.L. Choy, Spider silk binder for Si-based anode in lithium-ion batteries, Mater. Design 191 (2020) 108669.
[11] A. Su, J. Li, J. Dong, D. Yang, G. Chen, Y. Wei, An Amorphous/Crystalline Incorporated Si/SiO_x Anode material derived from biomass corn leaves for lithium-ion batteries, Small 16 (2020) 2001714.
[12] J.R. Szczech, S. Jin, Nanostructured silicon for high capacity lithium battery anodes, Energy Environ. Sci. 4 (2011) 56–72.
[13] S. He, S. Huang, S. Wang, I. Mizota, X. Liu, X. Hou, Considering critical factors of silicon/graphite anode materials for practical high-energy lithium-ion battery applications, Energy Fuels 35 (2) (2021) 944–964.
[14] Z. Guo, H. Yao, Thickness gradient promotes the performance of Si-based anode material for lithium-ion battery, Mater. Design 195 (2020) 108993.
[15] S.-S. Lee Ki-H. Nam, H. Jung, C.M. Park, Si-based composite interconnected by multiple matrices for high-performance Li-ion battery anodes Chem. Eng. Technol. 381 (2020) 122619.
[16] C.K. Chan, H. Peng, G. Liu, K. McIlwrath, X.F. Zhang, R.A. Higgins, Y. Cui, High-performance lithium battery anodes using silicon nanowires, Nat. Nanotech. 3 (2008) 31–35.
[17] A. Wang, S. Kadam, H. Li, S. Shi, Y. Qi, Review on modeling of the anode solid electrolyte interphase (SEI) for lithium-ion batteries, NPJ Comput. Mater. 15 (2018) 1–26.
[18] O. Pérez-Díaz, E. Quiroga-González, S. Hansen, N.R. Silva-González, J. Cartensen, R. Adelung, Fabrication of silicon microwires by a combination of chemical etching steps and their analysis as anode material in Li-ion batteries, Mater. Technol. 1–7 (2019).
[19] E. Quiroga, J. Carstensen, H. Föll, Good cycling performance of high-density arrays of Si microwires as anodes for Li ion batteries, Elecrochim. Acta 101 (2013) 31–35.
[20] E. Quiroga, J. Carstensen, H. Föll, Optimal conditions for fast charging and long cycling stability of silicon microwire anodes for lithium-ion batteries, and comparison with the performance of other Si anode concepts, Energies 6 (2013) 5145–5156.
[21] J. Chen, X. Fan, Q. Li, H. Yang, M.R. Khoshi, Y. Xu, S. Hwang, L. Chen, X. Ji, C. Yang, H. He, C. Wang, E. Garfunkel, D. Su, O. Borodin, C. Wang, Electrolyte design for LiF-rich solid-electrolyte interfaces to enable high performance microsized alloy anodes for batteries, Nature Energy 5 (2020) 386–397.
[22] E. Peled, The electrochemical behavior of alkali and alkaline earth metals in nonaqueous battery systems - the solid electrolyte interphase model, J. Electrochem. Soc. 126 (1979) 2047–2051.
[23] P. Verma, P. Maire, P. Novák, A review of the features and analyses of the solid electrolyte interphase in Li-ion batteries, Electrochim. Acta 55 (2010) 6332–6341.
[24] M. Winter, The solid electrolyte interphase–the most important and least understood solid electrolyte in rechargeable Li batteries, Z. Phys. Chem. 223 (2009) 1395–1406.
[25] E. Peled, S. Menkin, Review—SEI: past, present and future, J. Electrochem. Soc. 164 (2017) A1703–A1719.
[26] F. Shi, P.N. Ross, Solid electrolyte interphase in lithium-based batteries, EIBC (2019).
[27] C. Cao, H.-G. Steinrück, B. Shyam, K.H. Stone, M.F. Toney, In situ study of silicon electrode lithiation with X-ray reflectivity, Nano letters 16 (12) (2016) 7394–7401.
[28] C. Cao, I.I. Abate, E. Sivonxay, B. Shvam, C. Jia, B. Moritz, T.P. Devereaux, K.A. Persson, H.-G. Steinrück, M.F. Toney, Solid electrolyte interphase on native oxide-terminated silicon anodes for Li-ion batteries, Joule 3 (2018) 1–20.
[29] Bard, A.J.; Faulkner, L.R. Electrochemical Methods: Fundamentals and Applications, 2nd ed., John Wiley & Sons Inc. 2001, New York.
[30] S. Hansen, E. Quiroga-González, J. Carstensen, R. Adelung, H. Föll, Size-dependent physicochemical and mechanical interactions in battery paste anodes of Si-microwires revealed by fast-fourier-transform impedance spectroscopy, J. Power Sources 349 (2017) 1–10.
[31] E. Ivers-Tiffée, A. Weber, Evaluation of electrochemical impedance spectra by the distribution of relaxation times, J. Ceram. Soc. Jpn. 125 (2017) 193–201.
[32] M.A. Danzer, Generalized distribution of relaxation times analysis for the characterization of impedance spectra, Batteries 5 (2019) 53.
[33] M. Hahn, S. Schindler, L.-C. Triebs, M.A. Danzer, Optimized process parameters for a reproducible distribution of relaxation times analysis of electrochemical systems, Batteries 5 (2019) 43.
[34] B.A. Boukamp, A. Rolle, Analysis and application of distribution of relaxation times in solid state ionics, Solid State Ion. 302 (2017) 12–18.
[35] H. Schichlein, A.C. Müller, M. Voigts, A. Krügel, E. Ivers-Tiffée, Deconvolution of electrochemical impedance spectra for the identification of electrode reaction mechanisms in solid oxide fuel cells, J. Appl. Electrochem. 32 (2002) 875–882.
[36] V. Sonn, A. Leonide, E. Ivers-Tiffée, Combined deconvolution and CNLS fitting approach applied on the impedance response of technical Ni/8YSZ cermet electrodes, J. Electrochem. Soc. 155 (2008) B675–B679.

[37] A. Weiß, S. Schindler, S. Galbiati, M.A. Danzer, R. Zeis, Distribution of relaxation times analysis of high-temperature PEM fuel cell impedance spectra, Electrochim. Acta. 230 (2017) 391–398.
[38] D. Papurello, D. Menichini, A. Lanzini, Distributed relaxation times technique for the determination of fuel cell losses with an equivalent circuit model to identify physicochemical processes, Electrochim. Acta 258 (2017) 98–109.
[39] B.A. Boukamp, A. Rolle, Use of a distribution function of relaxation times (DFRT) in impedance analysis of SOFC electrodes, Solid State Ion. 314 (2018) 103–111.
[40] J.P. Schmidt, P. Berg, M. Schönleber, A. Weber, E. Ivers-Tiffée, The distribution of relaxation times as basis for generalized time-domain models for Li-ion batteries, J. Power Sources 221 (2013) 70–77.
[41] S. Gantenbein, M. Weiss, E. Ivers-Tiffée, Impedance based time-domain modeling of lithium-ion batteries: Part I, J. Power Sources 379 (2018) 317–327.
[42] W. Li, Y. Li, X. Yao, M. Fang, M. Shui, J. Shu, Y. Ren, Distribution of relaxation times investigation of Co^{3+} doping lithium-rich cathode material Li $[Li_{0.2}Ni_{0.1}Mn_{0.5}Co_{0.2}O_2$, Bull. Mater. Sci. 41 (2018) 155.
[43] M. Saccoccio, T.H. Wan, C. Chen, F. Ciucci, Optimal regularization in distribution of relaxation times applied to electrochemical impedance spectroscopy: Ridge and Lasso regression methods – A theoretical and experimental study, Electrochim. Acta 147 (2014) 470–482.
[44] T.H. Wan, M. Saccoccio, C. Chen, F. Ciucci, Influence of the Discretization Methods on the Distribution of Relaxation Times Deconvolution: Implementing Radial Basis Functions with DRTtools, Electrochim. Acta 182 (2015) 483–499.
[45] F. Ciucci, C. Chen, Analysis of electrochemical impedance spectroscopy data using the distribution of relaxation times: A Bayesian and hierarchical Bayesian approach, Electrochim. Acta 167 (2015) 439–454.
[46] M.B. Effat, F. Ciucci, Bayesian and hierarchical Bayesian based regularization for deconvolving the distribution of relaxation times from electrochemical impedance spectroscopy data, Electrochim. Acta 247 (2017) 1117–1129.
[47] L.S. Solís-Méndez, J.M. Baas-López, D.E. Pacheco-Catalán, J.A. Uribe-Calderón, Effect of polyaniline content on the electrochemical behavior of tin oxide/polyaniline composites by solution mixing, J Mater Sci: Mater Electron 32 (2021) 299–312.
[48] J. Guo, A. Sun, X. Chen, C. Wang, A. Manivannan, Cyclability study of silicon-carbon composite anodes for lithium-ion batteries, using electrochemical impedance spectroscopy, Electrochim. Acta 56 (2011) 3981–3987.
[49] H. Chen, Z. Wu, Z. Su, S. Chen, C. Yan, M. Al-Mamun, Y. Tang, S. Zhang, A mechanically robust self-healing binder for silicon anode in lithium ion batteries, Nano Energy 81 (2021) 105654.
[50] D. Yao, J. Feng, J. Wang, Y. Deng, C. Wang, Synthesis of silicon anode binders with ultra-high content of catechol groups and the effect of molecular weight on battery performance, J. Power Sources 463 (2020) 228188.
[51] K. Zhang, Y. Zhang, J. Zhou, Y. Li, B. Zheng, F. Yang, Y. Kai, A stress-based charging protocol for silicon anode in lithium-ion battery: Theoretical and experimental studies, J. Energy Storage 32 (2020) 101765.
[52] D. Liu, Y. Zhao, R. Tan, L.-L. Tian, Y. Liu, H. Chen, F. Pan, Novel conductive binder for high-performance silicon anodes in lithium ion batteries, Nano Energy 36 (2017).
[53] K. Kang, H.-S. Lee, D.-W. Han, G.-S. Kim, D. Lee, Maximum Li storage in Si nanowires for high capacity three-dimensional Li-ion battery, Appl. Phys. Lett. 96 (2010) 053110.
[54] S.Y. Lai, K.D. Knudsen, B.T. Sejersted, A. Ulvestad, J.P. Mæhlan, A.Y. Koposov, Silicon nanoparticle ensembles for lithium-ion batteries elucidated by small-angle neutron scattering, ACS Appl. Energy Mater. 2 (2019) 3220–3227.
[55] C.K. Chan, R. Ruffo, S.S. Hong, R.A. Huggins, Y. Cui, Structural and electrochemical study of the reaction of lithium with silicon nanowires, J. Power Sources 189 (2009).
[56] M. Ge, J. Rong, X. Fang, A. Zhang, Y. Lu, C. Zhou, Scalable preparation of porous silicon nanoparticles and their applications for lithium-ion battery anodes, Nano Res. 6 (2013) 174–181.
[57] Q. Ma, Z. Zhao, Y. Zhao, H. Xie, P. Xing, D. Wang, H. Yin, A self-driven alloying/dealloying approach to nanostructuring micro-silicon for high-performance lithium-ion battery anodes, Energy Storage Mater. 34 (2021) 768–777.
[58] J. Wu, J. Liu, Z. Wang, X. Gong, Y. Wang, A new design for Si wears double jackets used as a high-performance lithium-ion battery anode, Chem. Eng. J. 370 (2019) 565–572.
[59] S. Sim, P. Oh, S. Park, J. Cho, Critical thickness of SiO_2 coating layer on core@shell bulk@nanowire Si anode materials for Li-ion batteries, Adv. Mater. 25 (2013) (2013) 4498–4503.
[60] C. Cao, B. Shyam, J. Wang, M.F. Toney, H.G. Steinrück, Shedding X-ray light on the interfacial electrochemistry of silicon anodes for Li-ion batteries, Acc. Chem. Res. 52 (2019) 2673–2683.
[61] J.W. Choi, J. McDonough, S. Jeong, J.S. Yoo, C.K. Chan, Y. Cui, Stepwise nanopore evolution in one-dimensional nanostructures, Nano letters 10 (2010) 1409–1413.
[62] E. Quiroga-González, J. Carstensen, H. Föll, Structural and electrochemical investigation during the first charging cycles of silicon microwire array anodes for high capacity lithium ion batteries, Materials 6 (2013) 626–636.
[63] E. Quiroga-González, E. Ossei-Wusu, J. Carstensen, H. Föll, How to make optimized arrays of Si wires suitable as superior anode for Li-ion batteries, J. Electrochem. Soc. 158 (11) (2011) E119–E123.
[64] G.M. Veith M. Doucet R.L. Sacci B. Vacaliuc J. Kevin Baldwin J.F. Browning Determination of the solid electrolyte interphase structure grown on a silicon electrode using a fluoroethylene carbonate additive Sci. Rep. 7 (2017+) 6326.
[65] J.S. Ko, M.B. Sassin, D.R. Rolison, J.W. Long, Deconvolving double-layer, pseudocapacitance, and battery-like charge-storage mechanisms in nanoscale $LiMn_2O_4$ at 3D carbon architectures, Electrochim. Acta 275 (2018) 225–235.
[66] J. Ko S., C.-H. Lai, J. Long W., D. Rolison R., B. Dunn, J. Nelson Weker, Differentiating double-layer, pseudocapacitance, and battery-like mechanisms by analyzing impedance measurements in three dimensions, ACS Appl. Mater. Interfaces 12 (12) (2020) 14071–14078.
[67] J. Ko S., M. Sassin B., D. Rolison R., J. Long W., Combining battery-like and pseudocapacitive charge storage in 3D MnOx@carbon electrode architectures for zinc-ion cells, Sustainable Energy Fuels 2 (2018) 626–636.